Macromolecular Materials and Engineering

Macromolecular Materials and Engineering Open Access

www.mame-journal.de

RESEARCH ARTICLE OPEN ACCESS

Dual-Phytocompound-Loaded Polycaprolactone Nanoparticles: Formulation, Characterization, In Vitro Antioxidant and Antitumor Evaluation

Cyril Tlou Selepe[1,2] | Khanyisile Sheer Dhlamini[1,2] | Lesego Tshweu[1,3] | Zandile Nxumalo[4] | Nkoana Ishmael Mongalo[5] | Maropeng Vellry Raletsena[5] | Lusisizwe Kwezi[6] | Bathabile Ramalapa[1,3] | Suprakas Sinha Ray[1,2,7]

[1]Biotherapeutics Delivery Laboratory, Centre For Nanostructures and Advanced Materials, DSI-CSIR Nanotechnology Innovation Centre, Council for Scientific and Industrial Research, Pretoria, South Africa | [2]Department of Chemical Sciences, University of Johannesburg, Johannesburg, South Africa | [3]Material Science, Innovation and Modeling (MaSIM), Faculty of Natural and Agricultural Sciences, North-West University, Mmabatho, South Africa | [4]Synthetic Nanobiotechnology and Biomachines Group, Synthetic Biology and Precision Medicine Centre, CSIR, Pretoria, South Africa | [5]College of Agriculture and Environmental Sciences, Department of Agriculture and Animal Health, CAES Laboratories, University of South Africa, Florida, South Africa | [6]Biomanufacturing Technology Demonstration Group, Council for Scientific and Industrial Research, Pretoria, South Africa | [7]College of Material, Chemistry, and Chemical Engineering, Hangzhou Normal University, P. R. China

Correspondence: Bathabile Ramalapa (bramalapa@csir.co.za) | Suprakas Sinha Ray (rsuprakas@csir.co.za)

Received: 21 November 2025 | **Revised:** 26 January 2026 | **Accepted:** 9 February 2026

Keywords: antitumour activity | betulinic acid | nanodelivery systems | polycaprolactone | taraxerol

ABSTRACT

Betulinic acid (BA) and taraxerol (TA) have gained attention for their potent pharmacological antioxidant and antitumor properties. However, their poor water solubility limits clinical use. In this study, polycaprolactone (PCL) nanocarriers were prepared via a single emulsion–solvent evaporation method to co-encapsulate BA and TA, thereby improving their solubility, stability, and bioavailability. The resulting particles had an average size of 261 ± 7.70 nm and a zeta potential of −18.00 ± 0.21 mV. Encapsulation efficiency was 82.77% for BA and 69.84% for TA, with drug loadings of 6.57 ± 0.45% and 5.54 ± 0.23%, respectively. XRD study confirmed the formulation's amorphous state, which favors drug dissolution, and TEM showed a spherical shape. In vitro release tests revealed a biphasic pattern: an initial burst followed by sustained release. The co-encapsulated nanocarriers exhibited enhanced antioxidant activity compared to free and individually encapsulated compounds, as shown by improved free radical scavenging. Additionally, the nanoformulation demonstrated significant antiproliferative effects against HepG2 and HeLa cell lines, indicating strong antitumor potential. These results suggest that PCL nanocarriers co-loaded with BA and TA provide a versatile and effective platform to enhance the therapeutic effects of natural triterpenoids, with promising applications for managing oxidative stress–related conditions and cancer.

1 | Introduction

Oxidative stress is a process that plays a key role in various diseases, such as cancer. It occurs when there is an imbalance between the production of reactive oxygen and nitrogen species (ROS/RNS) and their elimination by the body's intrinsic antioxidant systems. This imbalance can lead to irreversible cell damage and death, as free radicals attack cells [1]. Oxidative stress can worsen chronic inflammation by activating various transcription factors involved in inflammatory processes, leading to the release of inflammatory cytokines and chemokines. Simultaneously, inflammation triggers the overproduction of reactive oxygen

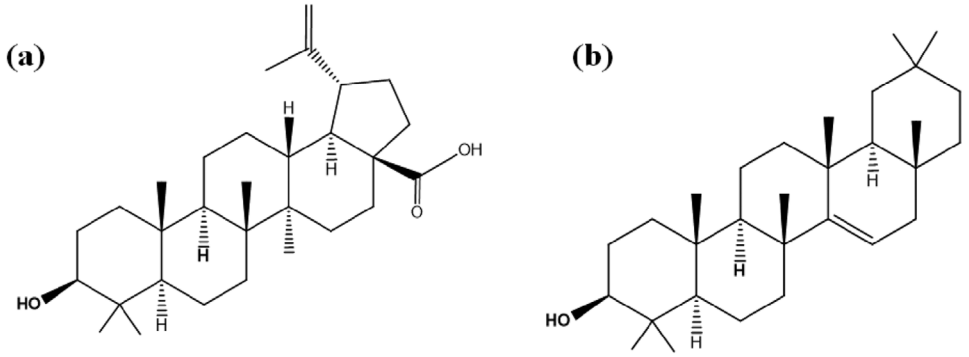

FIGURE 1 | Chemical structure of (a) betulinic acid (BA) and (b) taraxerol (TA).

species (ROS) and reactive nitrogen species (RNS), which further oxidize cellular biomolecules, leading to oxidative stress and tissue damage. Oxidative stress and inflammation often coexist, creating a cycle in which ROS promotes inflammation and, in turn, produces more ROS, further increasing cellular damage [2]. Over time, this environment can lead to carcinogenesis, contributing to the initiation, promotion, and progression of tumors.

Over the years, natural compounds such as betulinic acid (BA) and taraxerol (TA) have shown promising anticancer, antioxidant, and anti-inflammatory effects in various in vitro and in vivo studies [3]. Additionally, it is important to note that natural products and their derivatives account for more than one-third of the top-selling pharmaceuticals worldwide, underscoring their historically significant contribution to pharmaceutical development [4]. BA is a lupane-structured pentacyclic triterpene derived from various botanical sources, such as fruits and vegetables distributed throughout the plant kingdom. However, higher amounts of this compound can be extracted from the birch tree, mainly *Betula alba*. BA [5], and its derivatives exhibit a wide range of pharmacological activities, including antimalarial, anti-inflammatory, anti-HIV, anticancer, antidepressant, and antioxidant effects [6, 7]. Studies consistently show that it also has strong anticancer activity against various cancer cell lines, including breast, prostate, and colorectal cancers [8, 9]. The mechanism involves inducing cancer cell death through mitochondrial membrane permeabilization, which releases factors such as cytochrome c, Smac (second mitochondria-derived activator of caspases), or AIF (apoptosis-inducing factor), in a manner dependent on the permeability transition pore. This process activates caspases, leading to nuclear fragmentation [10, 11].

Similarly, TA, an oleanane-type pentacyclic triterpene, is another natural compound with significant potential for drug development. It has attracted widespread attention for its possible use as a therapeutic agent for treating various diseases [12, 13]. It is worth noting that *Hypericum perforatum*, *Clitoria ternatea*, *Mangifera indica*, and *Strobilanthes crispus* are among the leading plant sources of TA [14]. Research on TA has received considerable interest from scientists due to its substantial potential in pharmacology, including its ability to act as an antitumor, antimicrobial, and anti-inflammatory agent, as well as in the treatment of Alzheimer's disease [15–18]. The chemical structures of BA and TA are shown in Figure 1.

Despite having excellent anticancer properties, these compounds face several limitations, including poor water solubility and a short half-life, which diminish their efficacy and potential [19, 20]. To overcome the limitations of BA and TA, researchers have explored various approaches to improve their physicochemical and biopharmaceutical properties, such as encapsulating them in nanocarrier-based drug delivery systems, including liposomes and polymeric nanoparticles (PNPs) [21, 22]. Therefore, developing an effective delivery system is essential to address these issues and enhance sustained solubility, bioavailability, and targeted delivery of BA and TA as potent anticancer agents. Among these systems, PNPs have gained popularity as suitable drug carriers and are often made from biodegradable polymers such as poly(ε-caprolactone) (PCL). PCL is a synthetic, biodegradable, and biocompatible polymer frequently used in nanoparticle formulations. It is an affordable material approved by the US Food and Drug Administration (FDA) [23–25].

The ability of PCL to effectively deliver various drugs to target sites has been extensively studied [26, 27]. Hanie Ahmadi and colleagues reported the development of curcumin-loaded PCL NPs prepared by the emulsion–evaporation method, stabilized with a pH-responsive emulsifier. Their study showed improved NP stability, high encapsulation efficiency, and controlled pH-triggered release of curcumin, highlighting the system's potential for targeted drug delivery applications [28]. M. Luisa et al. [29] found that curcumin-loaded PCL NPs exhibit significant antioxidant and cytoprotective effects under oxidative stress conditions. Their research demonstrated that encapsulation in PCL enhances curcumin's stability and bioavailability, thus boosting its effectiveness against reactive oxygen species (ROS)- induced cellular damage.

On the other hand, Cabeza et al. [30] reported that doxorubicin encapsulated in PCL NPs showed improved antitumor activity and reduced systemic toxicity in both lung and breast cancer (BC) models. Their study, which included extensive in vitro and in vivo assessments, demonstrated that PCL-based NPs improve drug delivery efficiency, sustain drug release, and reduce adverse effects, highlighting their potential as safer and more effective chemotherapeutic carriers [30].

Despite many studies focusing on a limited set of natural compounds such as curcumin and quercetin, a growing body of evidence shows that PCL NPs and other PCL-based nanomaterials can improve the solubility, stability, and therapeutic activity

of various compounds. Notably, other promising phytochemicals, such as BA and additional polyphenols, have limited PCL-based reports, and co-delivery strategies are underdeveloped and poorly optimized [21]. This study builds on these findings to further optimize PCL-based delivery systems for these triterpenoids, aiming to maximize their bioactivity and therapeutic potential against oxidative stress and tumor cells. The main goal is to improve the effectiveness of BA and TA for their antioxidant and antitumor activities using a co-loaded PCL NPs system. The co-loaded NPs showed that co-encapsulation increased antioxidant activity compared to single-loaded and free compounds. The anticancer potential of these NPs was tested in HeLa and HepG2 cells, revealing greater cytotoxicity and proliferation inhibition with the co-loaded formulation. These results highlight the synergistic effects of BA and TA when co-encapsulated, suggesting that PCL-based nanocarriers can serve as a promising platform for developing new therapeutic strategies against cancer and other diseases.

2 | Experimental Section

2.1 | Materials

Polycaprolactone (PCL, Mw 14 000), poly(vinyl alcohol) (PVA) 87–89% hydrolyzed (M_w 30–70 kDa), sodium chloride (NaCl) ≥ 99.0%, potassium chloride (KCl) ≥ 99.0%, sodium phosphate dibasic (Na_2HPO) ≥ 99.0%, potassium phosphate monobasic (KH_2PO_4) ≥ 99.0%, phosphate buffer saline (PBS), acetone (C_3H_6O) ≥ 99.5%, TWEEN 80 were purchased from Sigma-Aldrich. BA was purchased from DB Fine Chemicals Specialties, Johannesburg, and TA was extracted from the roots of *Grewia flava DC*. Distilled water was used to prepare all the solutions. All reagents were of analytical grade and used as received without further purification.

2.1.1 | Plant Material and Extraction of TA

The roots of *Grewia flava L.* (*Malvaceae*) were collected from Pickup Farm (Latitude 23° 9′ 60″ South Longitude 29° 4′ 59″ East), near the Tswatsane River, in Limpopo Province, South Africa. A voucher specimen was also collected and verified by the National Biodiversity Institute in Pretoria, and the voucher (MongaloNI 24) specimen was lodged at the University of South Africa, Science Campus, Florida Park, Johannesburg. The roots were washed with tap water, rinsed with distilled water, dried on a laboratory workbench at 25°C, and ground into a 2 mm mesh size using a Scientec Hammer mill. Approximately 3 kg of finely ground plant material was submerged in acetone at a 1:5 (w/v) ratio and shaken on an incubator shaker (Already Enterprise Inc., LM-600 RD, Taiwan) at 120 rpm for 4 days. The plant material was filtered through Whatman's No. 1 filter paper. The liquid extract was then evaporated to dryness using a rotary evaporator at 40°C, yielding 28.95 g of plant extract [31].

2.1.2 | Fractionation and Isolation of Compound

The extract obtained was then subjected to solvent-solvent fractionation, using a method adopted from Suffness and Duros [32]. The extract was subjected to solvent-solvent fractionation using 1:1 chloroform: hexane to defat the extract. The chloroform fraction was further reduced to dryness using a rotary evaporator, yielding 19.55 g of the extract, which was subjected to column chromatography using silica gel as the stationary phase and hexane: ethyl acetate (9:1) as the mobile phase. TLC was used to monitor the fractions collected from the column. Fractions 56 to 78 resulted in a whitish compound (A), while fractions 94 to 109 resulted in a light brownish compound (B).

2.2 | Preparation of PCL-Loaded BA and TA NPs

PCL-loaded BA and TA NPs were prepared using the single emulsion solvent evaporation method with slight modifications [33]. Briefly, 20 mg of PCL and 10 mg of BA or TA were dissolved or co-dissolved in 2 mL of acetone, followed by the addition of 50 µL of TWEEN 80 to form the organic phase. The aqueous phase consisted of 2% (w/v) PVA and PBS buffer (pH = 7.4) in 10 mL, and both phases were homogenized separately under stirring for 5 min. The organic phase was then added dropwise into the continuously stirred aqueous phase to create a stable oil-in-water (O/W) emulsion. Acetone was subsequently removed by continuous stirring at room temperature, resulting in PCL-BA NPs, PCL-TA NPs, and PCL-BA-TA NPs, respectively. The NPs were collected by centrifugation at 14 200 g for 20 min at 4°C (Allegra 64R centrifuge, BECKMAN COULTER) and washed repeatedly with deionized water to remove residual PVA and unencapsulated drugs. The resulting pellets were frozen at −80°C and lyophilized using a Telstar LyoAlfra10 freeze-dryer (Spain) at −60°C and 0.3 mBar to obtain dry NP powders. PCL NPs were synthesized following the same method without the addition of BA or TA.

2.3 | Physicochemical Characterization

Drug loading and release were determined using a UV/vis spectrophotometer (UV-5, Mettler Toledo, Greifensee, Switzerland) and HPLC (Shimadzu Nexera, Japan). Measurements of particle size, polydispersity index (PDI), and zeta potential were carried out with the ZETASIZER Nano series (MALVERN INSTRUMENTS, Worcestershire, UK). These measurements were performed on diluted samples at 25 C, with each sample measured in triplicate. The data are presented as the mean ± standard deviation (SD). Attenuated Total Internal Reflectance-Fourier transform infrared spectroscopy (ATR-FTIR; PerkinElmer, Inc., Shelton, CT, USA) was conducted over the wavenumber range of 500–4000 cm^{-1} with a resolution of 4 cm^{-1}, and 32 scans were recorded for each experiment. Approximately 2 mg of each sample was placed on the FTIR plate for measurement, and all spectra were recorded against the background of the air spectrum. Structural elucidation and confirmation were assessed by ^{1}H and ^{13}C nuclear magnetic resonance (NMR) spectroscopy on a Varian Mercury 600 MHz NMR spectrometer (Varian, USA). The NMR samples of BA and TA were prepared in dimethyl sulfoxide-d6 and deuterated chloroform, respectively. X-ray diffraction (XRD) (X'Pert PRO Malvern PANalytical, UK) patterns of BA, TA, PCL, PCL NPs, PCL-BA NPs, and PCL-TA NPs were obtained using Cu Kα radiation (λ = 0.15405 nm) to produce measurements in the 2θ range of 5 to 90° at 45 kV and 40 mA. The powder samples were evenly spread on an XRD sample holder, with the surface flattened to ensure consistent diffraction. For bulk solid

(foam-like samples), an adhesive was used to hold the sample in place, ensuring a flat surface for XRD analysis. Transmission electron microscopy (TEM, JEM-2100, JEOL, Tokyo, Japan) operated at 200 kV was used to determine the internal morphology of PCL NPs, PCL-BA NPs, PCL-TA NPs, and PCL-BA-TA NPs. The samples were prepared by depositing a drop of their suspension onto a carbon-coated copper grid and drying at room temperature before observation. The thermal properties of PCL, PCL NPs, PCL-BA NPs, PCL-TA NPs, and PCL-BA-TA NPs were measured using a differential scanning calorimeter (DSC, model Q2000, TA Instruments, USA). The dried samples, weighing 5–6 mg, were loaded and sealed into an aluminum pan, then scanned from −10 to 450 C at 10 C/min under a continuous nitrogen purge.

2.4 | Drug Loading and Encapsulation Efficiency

To assess the drug loading capacity of PCL-BA NPs and PCL-TA NPs, methanolic stock solutions of BA and TA were prepared and analyzed using high-performance liquid chromatography (HPLC) (Shimadzu Nexera, Japan). The goal was to determine the total amount of drug encapsulated within the polymeric nanocarrier. A calibration curve was created through successive dilutions of the stock solution. HPLC analysis was conducted using a C18 column (Lichrosphere RP-18, 250 mm × 4 mm × 5 μm) operated at 30°C with a UV detector set at 210 nm. The mobile phase consisted of acetonitrile and methanol (80:20% v/v) with a flow rate of 0.5 mL/min. To measure encapsulation capacity, samples of PCL-BA NPs and PCL-TA NPs were dispersed in a water-methanol (1:1) mixture to produce sample solutions. These samples were centrifuged for 30 min at 4°C at 14 200 g, separating the supernatant for absorbance measurement. The drug loading capacity (%DL) and encapsulation efficiency (%EE) were calculated using the following formulas:

$$\%\mathrm{DL} = \frac{mass\ of\ drug\ within\ the\ NPs}{mass\ of\ NPs} \times 100\% \quad (1)$$

$$\%\mathrm{EE} = \frac{mass\ of\ drug\ loaded\ within\ the\ NPs}{mass\ of\ drug\ in\ the\ initial\ formulation} \times 100\% \quad (2)$$

2.5 | In Vitro Release Study

In vitro release of the BA and TA from PCL-BA NPs and PCL-TA NPs was studied in PBS solution at a physiological pH of 7.4. The purpose was to determine the amount of drug released at specific time points; therefore, achieving complete dissolution was essential for accurate measurement. The samples were incubated at 37 C in PBS buffer (1 mg/mL), and aliquots were collected at various time intervals. These aliquots were centrifuged at 21 400 g for 15 min at 4 C to remove NP debris and avoid interference with drug analysis. The supernatant containing the drug was diluted with methanol to ensure complete dissolution before HPLC analysis.

2.6 | Radical Scavenging Activity Using DPPH Assay

The DPPH radical scavenging assay was conducted according to the modified method recently described by Lebeloane et al. [34] Briefly, the absorbance of the DPPH solution was adjusted to 0.90–1.00 at 517 nm. Then, 160 μL of the prepared DPPH solution was mixed with 40 μL of the samples at various concentrations (1–0.003 mg/mL). The reaction mixture was incubated in the dark for 30 min, after which the absorbance was measured at 517 nm using a Biotek microplate reader (USA) [35]. A lower absorbance indicates a higher potential for free radical scavenging.

The percentage of radical scavenging activity was calculated using the formula:

$$\%\ \text{Scavenger Activity} = \left\{ \frac{(A_O - A_S)}{A_O} \right\} \times 100\% \quad (3)$$

where AO represents the absorbance of the control (DPPH solution without the sample), and AS represents the absorbance of the sample (DPPH solution with the sample).

The IC_{50} value (the concentration needed to inhibit 50% of DPPH radicals) was calculated using non-linear regression analysis by plotting scavenging activity percentage against the logarithm of sample concentrations. Ascorbic acid was used as a positive control. Each experiment was performed in triplicate, and results are presented as mean ± standard deviation (SD).

2.7 | Metal Chelation Assay

The metal chelation activity of the test samples was assessed using the ferrous ion (Fe^{2+}) chelation assay as described by Dinis et al. [36] with slight modifications. Briefly, 1 mL of each sample solution at different concentrations was mixed with 3.7 mL of deionized water and 0.1 mL of 2 mM $FeCl_2$ solution. The reaction was started by adding 0.2 mL of 5 mM ferrozine solution, followed by vigorous vortexing. The mixture was then incubated at room temperature in the dark for 10 min to allow the formation of the ferrous–ferrozine complex.

The absorbance of the resulting solution was measured at 562 nm using a UV–vis spectrophotometer. A control containing all reagents except the test sample (replaced with deionized water) was prepared in parallel. EDTA was used as a positive control. All measurements were conducted in triplicate, and results were expressed as mean ± SD.

The metal chelating activity (%) was calculated using the following equation:

$$\%\text{Chelation Activity} = \left\{ \frac{(A_C - A_S)}{A_C} \right\} \times 100\% \quad (4)$$

whereas AC are the absorbance values of the sample and control, respectively.

2.8 | Cell Culture, Growth Conditions, and Treatment Conditions

Human hepatocellular carcinoma (HepG2) and Henrietta Lacks (HeLa) cancer cell lines were used to evaluate the cytotoxicity and anticancer effects of BA, TA, PCL-BA NPs, and PCL-TA NPs.

Cells were cultured in 75 cm^2 flasks (Thermo Fisher Scientific, South Africa) and maintained in Dulbecco's Modified Eagle Medium (DMEM) supplemented with 10% (v/v) fetal bovine serum (FBS) and 1% penicillin-streptomycin (200 U/mL penicillin and 270 µg/mL streptomycin). Cultures were incubated at 37 °C in a humidified atmosphere containing 5% CO_2. Cells were subcultured three times upon reaching approximately 90% confluency, and the cells were used in cytotoxicity assays.

2.9 | Cytotoxicity Assessment and Anti-Cancer Activity

The cytotoxicity assay and anti-cancer activity of the samples were conducted by first seeding HepG2 and HeLa cells in a 96-well plate and incubating them for 24 h at 37°C with 5% CO_2. After the 24-h incubation, a 2-fold serial dilution was performed using free BA and TA in 0.1% DMSO, free NPs, and reformulated BA and TA in PBS, starting at 1 mg/mL. To the wells containing cells, 100 µL of the serially diluted samples were added, except in the control wells. After 48 h of incubation, the media was removed and replaced with 25 µL of MTT reagent (5 mg/mL; Sigma-Aldrich, St. Louis, MO). The formazan product was then allowed to form from viable cells during a 3-h incubation at 37°C. Following incubation, the MTT reagent was removed, and 100 µL of DMSO was added, followed by a 15-min incubation at 25°C. The microplate was then read at 620 nm using the Tecan Infinite F500 luminometer. Experiments were performed in triplicate.

2.10 | Statistical Analysis

The experimental methods were performed independently three times, and the results were reported as averages across these three trials. The cytotoxicity data were analyzed using GraphPad Prism 8.

3 | Results and Discussion

3.1 | Isolation and Characterization of TA and BA

Here, we isolated TA from the root extract of Grewia Flava. The isolation was carried out using column chromatography, starting with vacuum column chromatography to separate and simplify compounds in the crude extract. The fraction obtained from vacuum column chromatography was further purified by gravity column chromatography, resulting in four subfractions. The structure of TA was identified and characterized using spectroscopic methods such as NMR, FTIR, and UV–vis, with comparisons to data from known compounds reported in the literature [14, 37, 38].

3.1.1 | Thin-Layer Chromatography (TLC) for Evaluation of TA and BA

TLC is a commonly used method for the qualitative analysis and separation of TA in plant extracts. It is a quick, cost-effective way to detect TA, often complemented by techniques such as NMR for additional confirmation. A simple, fast, and accurate TLC method was developed and validated to quantify TA in Grewia Flava [31]. A sharp, well-defined peak for TA at a retention factor (R_f) of 0.53 was observed, and the chromatogram is shown in Figure 2. In TLC, TA usually appears as a distinct violet, blue, or pink spot when treated with anisaldehyde-sulfuric acid spray reagent and heated. Its R_f falls between 0.3 and 0.6, depending on the solvent system. Because TA has weak UV absorption, it is best visualized using chemical staining. For BA, a single spot with an R_f of 0.45 was observed after treatment with the anisaldehyde–sulfuric acid reagent, producing a violet-blue color, as shown in the chromatogram. These chromatographic fingerprints are crucial for phytochemical standardization and support further structural and bioactivity research.

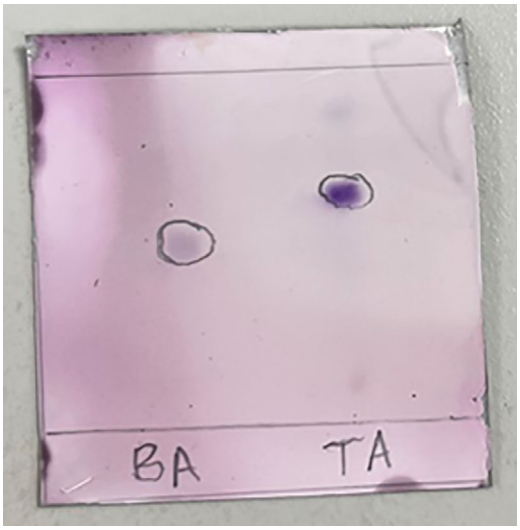

FIGURE 2 | Thin-layer chromatography (TLC) plate of betulinic acid (BA) and taraxerol (TA).

3.1.2 | UV–Vis Spectrometry of TA

UV–vis spectroscopy is a valuable method for analyzing TA and BA, pentacyclic triterpenoids found in various plant species. The UV–vis absorption spectra of BA and TA were recorded to examine their electronic transitions and structural characteristics. Both triterpenoids lack extensive conjugated systems; therefore, their absorption mainly occurs in the ultraviolet region due to $\pi \rightarrow \pi^*$ and $n \rightarrow \pi^*$ transitions of localized functional groups [39]. Figure 3 shows a single, consistent maximum absorption band for both TA and BA around 210 nm. In plant extracts, UV–vis spectroscopy is often combined with chromatographic techniques such as HPLC and TLC to confirm the presence of TA and BA. However, because of their weak UV absorption, supplementary techniques such as FTIR, NMR, and MS are also used for more definitive identification. In summary, both BA and TA absorb strongly in the deep-UV near 210 nm, with λ_{max} at approximately 210 nm being routinely used for quantitative analysis in formulations and mixtures [40, 41]. These results provide fundamental spectral data useful for purity assessment, formulation development, and further spectroscopic studies in nanocarrier encapsulation research.

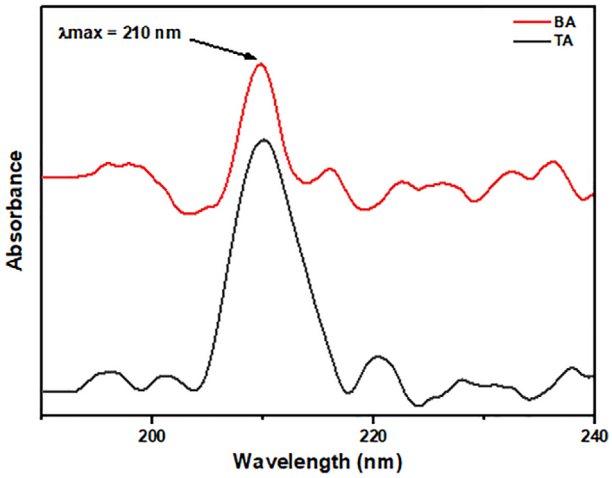

FIGURE 3 | UV–vis spectra of betulinic acid (BA) and taraxerol (TA).

3.1.3 | Structure Elucidation of TA and BA using NMR

Figure 4a shows the ^{1}H NMR spectrum ($CDCl_3$) of the *G. flava* extracted TA. The ^{1}H NMR spectrum of TA mainly displays eight tertiary methyl singlets from 0.79 to 1.2 ppm and a dense cluster of aliphatic methylene/methine signals from 0.8 to 2.69 ppm, due to the terpenoid protons. The lack of vinylic or oxymethine protons is consistent with TA and matches spectra reported for authentic standards and plant isolates. Additionally, the ^{1}H NMR spectrum reveals a key diagnostic feature: a single oxygenated methine at C-3, seen as a downfield signal at 3.19–3.20 ppm, indicating an axial H-3 next to a β-oriented hydroxyl group. This is confirmed by the double doublet at 3.20 ppm, confirming the OH group, and the methylene group is validated by the double doublet at 4.50 ppm. The signals at 4.90 and 4.74 ppm are assigned to the terminal alkenyl protons. A single olefinic proton, likely H-15, appears at 5.52–5.54 ppm, confirming a $\Delta^{14,15}$ double bond within the taraxerane skeleton rather than an isopropenyl exomethylene as seen in lupanes such as BA. These proton features are essential for confirming TA in phytochemical separations and authenticating TA in *G. flava* fractions. Likewise, Figure 4b presents the ^{1}H NMR spectrum (DMSO-d6) of BA. It displays distinct signals for its six methyl groups around 0.65–0.93 ppm, exomethylene protons at C-29 around 4.55–4.70 ppm, and the C-3 methine proton around 3.13–3.50 ppm. The methyl protons appear as singlets, the C-3 methine as a triplet or multiplet, and the C-29 protons as broad singlets. The ^{13}C NMR spectrum ($CDCl_3$) shown in Figure 5a displays distinct carbon signals from 0 to 220 ppm. The spectrum's features align with TA, consistent with previous literature describing this compound from *Myrica rubra* and *Euphorbia pubescens*. Sakurai et al. [42] reported TA from *Myrica spp*. (*Myrica rubra* & related species) among several triterpenoids from the bark. Valente et al. [43] identified TA within the terpenoid profile of *Euphorbia pubescens*. Similarly, the ^{13}C NMR spectrum (DMSO-d6) of BA in Figure 5b displays distinct carbon signals from 0–220 ppm, characteristic of methyl, methylene, methine, olefinic, quaternary, and carboxylic acid carbons. The five methyl groups are below 30 ppm, while the olefinic carbons of the isopropenyl group appear between 110 and 150 ppm. A clear signal for the carboxylic acid carbon appears around 170 ppm.

3.2 | Synthesis and Characterization of PCL-BA NPs, PCL-TA NPs, and PCL-BA-TA NPs

Using various characterization techniques is essential to determine the physicochemical properties of NPs — particle size, shape, distribution, and crystallinity — and to assess their safety for biomedical applications. The mean particle size, polydispersity index (PDI), zeta potential (ZP), and encapsulation efficiency of drug-free NPs and PCL-loaded NPs containing BA and TA are shown in Table 1. A low molecular weight PCL was chosen for preparing these NPs due to its beneficial properties, such as biocompatibility, non-toxicity, and a shorter biodegradation period compared to high molecular weight PCL, as extensively documented in the literature, thereby allowing faster release of the encapsulated compounds [44]. The DLS analysis of the NPs indicated a uniform particle distribution, with average particle diameters ranging from 211 to 261 nm. Studies have demonstrated that adjusting the drug-to-polymer mass ratio during NP formulation significantly affects NP size, with higher drug mass resulting in larger particles. This finding aligns with previous research, which shows that higher polymer concentrations result in larger NPs, consistent with the fact that the average hydrodynamic diameter of NPs increases with increased polymer concentration. These NPs have a low PDI value (<0.3), indicating a relatively narrow size distribution.

In addition to size and surface characteristics, drug loading and encapsulation efficiency are critical parameters reflecting the suitability of the formulation approach. BA and TA were loaded into PCL NPs primarily through hydrophobic interactions and physical entrapment within the polymeric matrix during nanoparticle formation. Owing to their lipophilic nature, both drugs preferentially partitioned into the hydrophobic PCL core, resulting in high encapsulation efficiencies. PCL-BA NPs exhibited a drug loading of 6.85 ± 0.61% with an encapsulation efficiency of 81.30 ± 0.13%, while PCL-TA NPs showed a loading of 5.90 ± 0.19% and encapsulation efficiency of 69.91 ± 0.26%. In co-loaded PCL-BA-TA NPs, BA achieved 6.57 ± 0.45% loading with 82.77 ± 0.11% encapsulation efficiency, whereas TA showed 5.54 ± 0.23% loading and 69.84 ± 0.18% encapsulation efficiency, indicating minimal competition during co-encapsulation. The high encapsulation efficiencies obtained confirm that the single-emulsion technique is a suitable and effective approach for incorporating these hydrophobic triterpenoids into PCL NPs. This method facilitated efficient drug–polymer interactions and stable entrapment within the polymeric core. The results demonstrate a facile, reproducible, and successful drug loading strategy for both single- and dual-drug-loaded PCL NP systems.

The stability of NPs was assessed by examining the zeta potential (ζ). Notably, NPs with zeta potentials above ± 60, ± 30, and ± 20 mV are classified as highly stable, stable, and partially stable colloidal suspensions, respectively [45]. Conversely, previous research has shown that NPs with ZP values within ±5 mV tend to aggregate due to weak electrostatic forces. In this study, all NPs displayed negative surface charge potentials ranging from −9.6 ± 0.7 to −18.9 ± 1.1 mV. The stability of this formulation is likely due to the use of PVA as a stabilizer, as prior research indicates that high-molecular-weight stabilizers, such as PVA, yield stable NPs with low ZP values [46]. Additionally, the negative surface charge of the NPs results from the presence of acidic

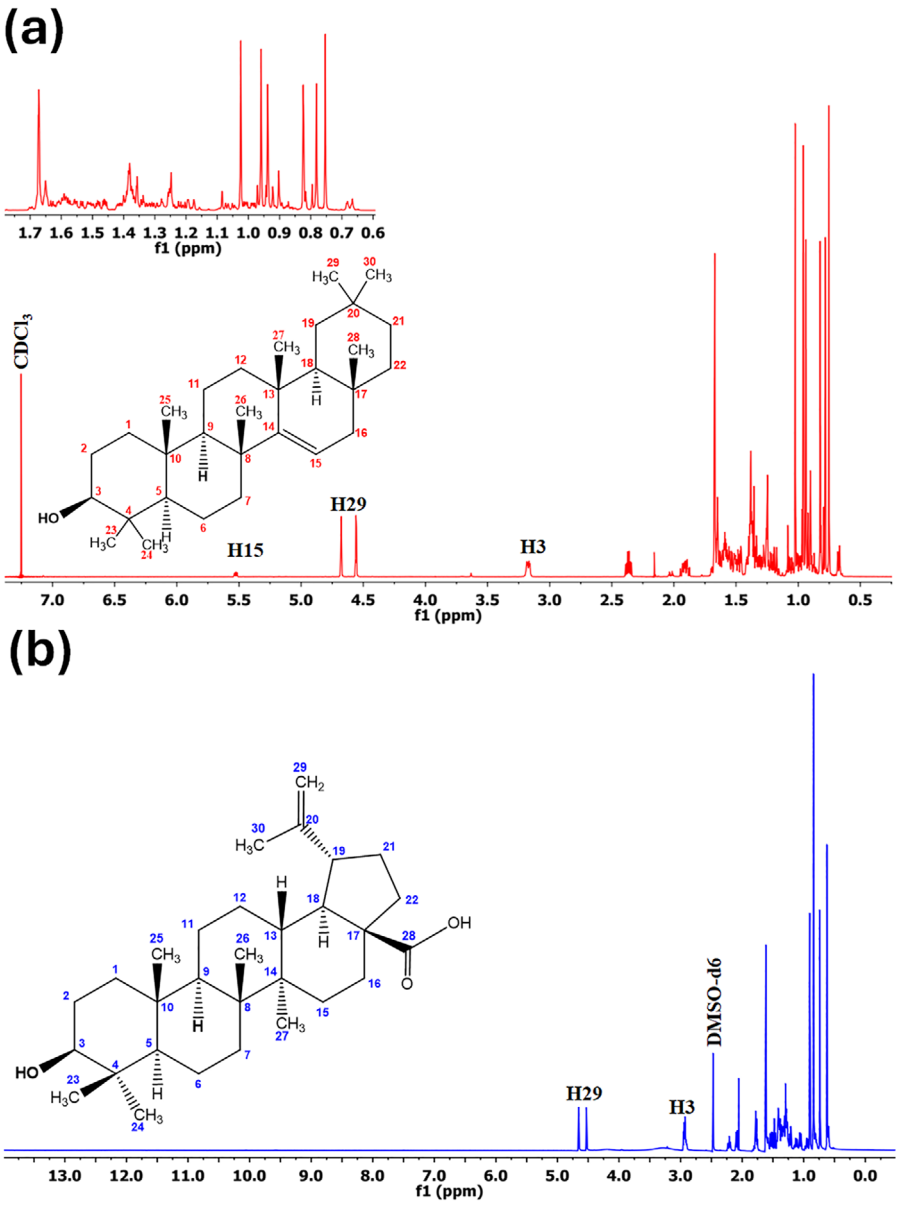

FIGURE 4 | The ^{1}H NMR spectra of: (a) taraxerol (TA) and (b) betulinic acid (BA).

carboxyl groups in PCL, which is important for targeted drug delivery.

FTIR was performed to confirm the successful encapsulation of BA and TA into polymeric nanoparticles by identifying absorption bands associated with specific functional groups. Figure 6 shows the FTIR spectra of BA, TA, PCL, PCL NPs, PCL-BA NPs, PCL-TA NPs, and PCL-BA-TA NPs. PCL displays characteristic absorption bands associated with its chemical structure, particularly its ester groups and aliphatic chains. It exhibits prominent peaks at 2939.2 and 2866.7 cm^{-1}, corresponding to the asymmetric and symmetric C—H stretching, respectively. A sharp peak at 1726.4 cm^{-1} indicates ester carbonyl (C═O) stretching, while another at 1231 cm^{-1} indicates C—O—C stretching from the ester bond (C—O) [47]. BA, which contains functional groups such as hydroxyl (OH) and carboxylic acid (—COOH), exhibits FTIR features characteristic of these groups. The peak at 1754 cm^{-1} corresponds to the carbonyl (C═O) of the carboxylic acid, and the peak at 1256.5 cm^{-1} relates to C—O stretching from the same group. The asymmetric and symmetric stretching of C—H groups appear at 2987.6 cm^{-1}, with a broad band around 3224.8 cm^{-1} indicating hydroxyl (-OH) groups [48]. TA, a pentacyclic triterpenoid similar to BA but lacking the carboxylic acid group, primarily features hydroxyl groups. Its FTIR spectrum shows signals from hydroxyl (—OH) and aliphatic ($—CH_2$, $—CH_3$) groups. The stretching vibration around 1050–1030 cm^{-1} corresponds to secondary alcohol (C—O), while bending vibrations of CH_2 and CH_3 groups are seen at 1450–1380 cm^{-1}. The asymmetric and symmetric stretching vibrations of CH_2 and CH_3 groups are observed at 2930–2870 cm^{-1}. Additionally, stretching vibrations at 3400–3450 cm^{-1} are associated with hydroxyl groups [49]. The FTIR spectrum of PCL NPs shows characteristic peaks similar to those of bulk PCL, with slight shifts or changes in intensity due to nanoparticle formation, which involves a smaller particle size, increased surface area, and interactions during encapsulation [50]. Notably, PCL-TA NPs exhibit a similar

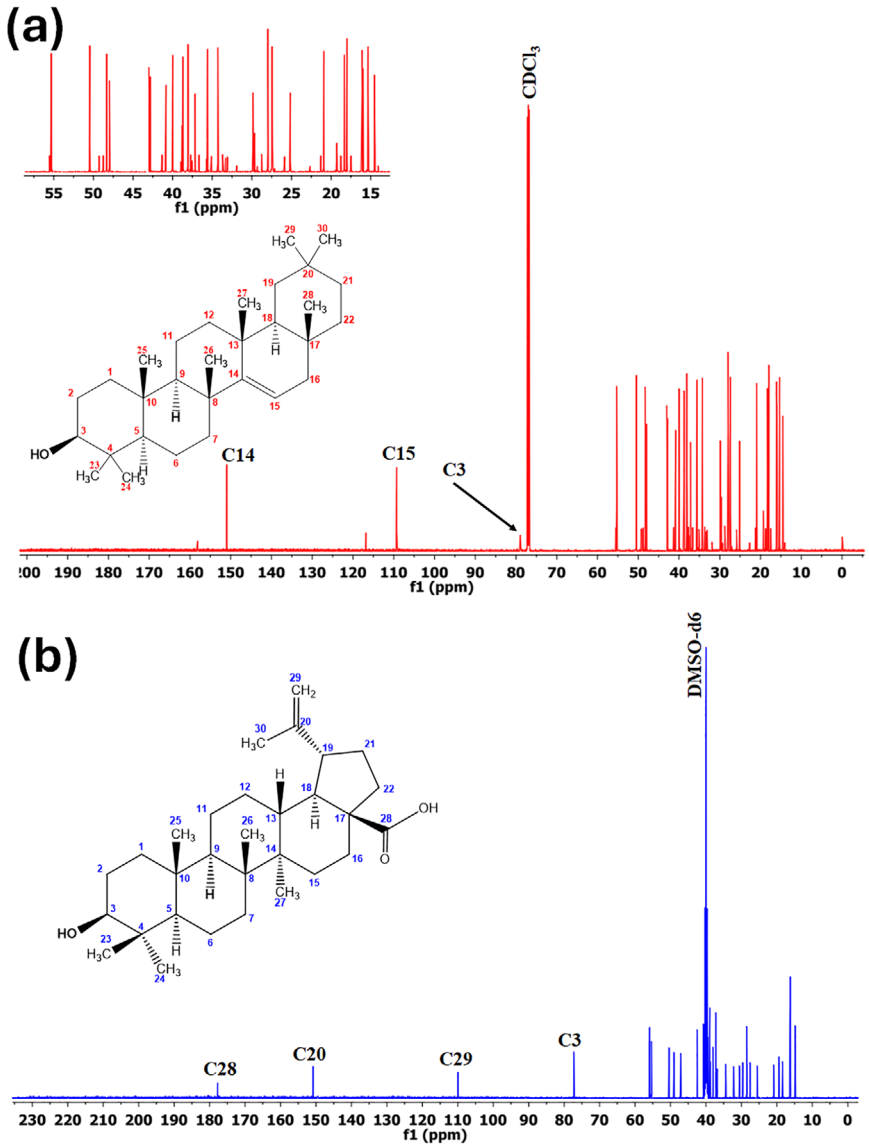

FIGURE 5 | The ^{13}C NMR spectra of: (a) taraxerol (TA) and (b) betulinic acid (BA).

absorption spectrum, with a broad peak at 3353.9 cm^{-1}, indicative of O—H stretching. Sharp peaks at 2866.7 cm^{-1} for symmetric C—H stretching, 1733 cm^{-1} for C═O stretching, and 1242 cm^{-1} for C—O—C stretching were also observed. The disappearance of some prominent peaks from the TA spectrum and the emergence of a new absorption peak in the PCL-TA NPs spectrum suggest successful integration of TA into the PCL matrix. The FTIR analysis indicates no chemical interactions between PCL and BA molecules within the PCL-encapsulated BA NPs. Furthermore, no BA characteristic peaks are observed in the PCL-BA NPs, implying efficient encapsulation of BA by the PCL matrix. A similar FTIR spectrum was observed for the PCL-BA-TA NPs, indicating comparable encapsulation behavior.

The crystalline or amorphous nature of PCL-BA NPs, PCL-TA NPs, and PCL-BA-TA NPs was compared with BA, TA, and PCL in their pure form using XRD, as shown in Figure 7. The XRD pattern of PCL displayed prominent diffraction peaks at 2θ angles of 17.37° and 19.64°, which correspond to the (110) and (200) planes of PCL's orthorhombic crystal structure [51]. Conversely, BA is a highly crystalline natural triterpenoid, and its XRD pattern exhibits multiple sharp, intense peaks indicating a well-ordered crystal structure. The presence of many sharp peaks across the low-to-mid 2θ range confirms its high crystallinity, with prominent peaks at 5.55°, 9.18°, 13.40°, 15°, and 22.64° [52]. Similarly, TA, another crystalline triterpenoid such as BA, generally shows fewer, broader peaks, suggesting lower crystallinity or different packing arrangements. The peaks are still distinguishable but may be less sharp or intense compared to BA, with notable peaks at 5.98°, 7.41°, 9.69°, and 13.45° [53]. It is important to note that the XRD pattern of PCL NPs reveals weaker and broader peaks compared to bulk PCL, indicating partial disruption of its crystalline structure due to the small particle size, rapid solvent evaporation during nanoemulsion, or the presence of drug molecules. The reduction in diffraction peak intensity suggests a more amorphous nature in the NPs. Additionally, this observation is supported by the DSC results, which indicate that both PCL-BA NPs and PCL-TA NPs exhibit amorphous forms. The absence of BA and TA peaks in the XRD patterns of PCL-BA NPs and PCL-TA NPs indicates that both

TABLE 1 | Physical-chemical properties of developed formulation (n = 3, mean ± SD).

Formulation	Size (nm)	PDI	ZP (mV)	BA EE%	BA Loading%	TA EE%	TA Loading%
PCL NPs	211 ± 9.11	0.206 ± 0.10	−9.66 ± 1.17	—	—	—	—
PCL-BA NPs	240 ± 6.18	0.214 ± 0.04	−10.50 ± 1.28	81.30±0.133	6.85±0.61	—	—
PCL-TA NPs	232 ± 9.81	0.270 ± 0.02	−11.73 ± 0.29	—	—	69.91 ± 0.26	5.90 ± 0.19
PCL-BA-TA NPs	261 ± 7.70	0.250 ± 0.01	−18.90 ± 0.21	82.77 ± 0.110	6.57 ± 0.45	69.84 ± 0.177	5.54 ± 0.23

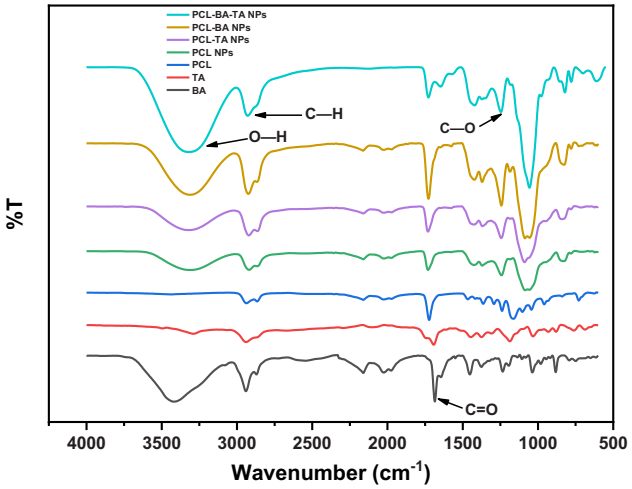

FIGURE 6 | FTIR spectra of BA, TA, PCL, PCL NPs, PCL-TA NPs, PCL-BA NPs, and PCL-BA-TA NPs.

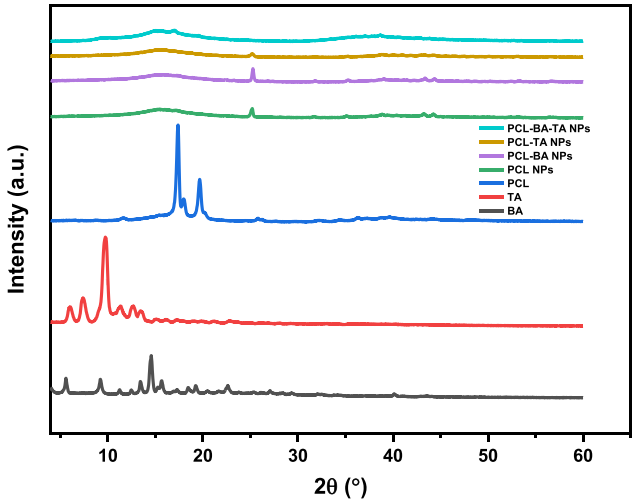

FIGURE 7 | XRD patterns of BA, TA, PCL, PCL NPs, PCL-BA NPs, PCL-TA NPs, and PCL-BA-TA NPs.

drugs are entrapped within the PCL matrix. The decrease in peak intensity or broadening suggests reduced crystallinity, mainly due to encapsulation and nanoscale dispersion. The nearly absent drug peaks point to amorphization within the polymer matrix. Crystalline BA and TA tend to have low solubility because their strong crystal lattices are challenging to break in biological fluids. In contrast, amorphous or molecularly dispersed drugs, as indicated by the lack of sharp peaks in XRD, possess higher energy states, increased apparent solubility, and faster dissolution rates. In summary, the XRD patterns of PCL-BA NPs, PCL-TA NPs, and PCL-BA-TA NPs show the disappearance of the characteristic sharp crystalline peaks of the free drugs, indicating a transition to an amorphous or molecularly dispersed form within the polymer matrix. This structural change enhances the apparent solubility and dissolution rate of the drugs, thereby improving their bioavailability and therapeutic effectiveness. These findings support the hypothesis that nanoparticle encapsulation can address the inherent solubility limitations of BA and TA.

TEM analysis and SAED patterns of PCL NPs, PCL-BA NPs, PCL-TA NPs, and PCL-BA-TA NPs are shown in Figure 8. The images display spherical particles with no visible lattice fringes, indicating a lack of long-range order at the nanoscale, as shown in Figure 8a–d. This suggests that the morphology of PCL NPs prepared by the single-emulsion method is typically spherical [54]. Meanwhile, selected-area electron diffraction (SAED) from the identical particles revealed broad, diffuse halo or ring features rather than sharp spots or narrow Debye–Scherrer rings, consistent with an amorphous or poorly ordered phase (Figure 8e–h). Most PCL NP systems show an amorphous halo or weak diffraction because the polymer matrix is not strongly crystalline at the nanoscale [55]. The absence of discrete lattice fringes in high-resolution TEM, along with diffused SAED patterns, supports the XRD results, which show significantly reduced PCL crystallinity or a predominantly amorphous pattern after NP formation and drug loading. The encapsulation of BA and TA in PCL disrupts polymer chain packing during solvent evaporation, reducing crystalline domains and creating amorphous matrices that trap the drugs, explaining the consistent TEM/SAED and XRD observations. The combined morphological evidence (absence of lattice fringes), diffraction data (diffuse SAED halos), and bulk XRD patterns (shown in Figure 7) all indicate that the NPs are largely amorphous, which has implications for drug release, as it is typically faster from amorphous matrices.

DSC analysis was performed to assess the thermal properties of BA, TA, PCL, PCL NPs, PCL-BA NPs, PCL-TA NPs, and PCL-BA-TA NPs. The thermograms of native BA and TA were recorded up to 400 °C to capture their full thermal transitions, including melting points and decomposition onset. This range was suitable, given the high thermal stability of these compounds in their free forms. However, for the PCL NPs and PCL-loaded formulations, the DSC analysis was limited to a maximum of 200°C. This limit was chosen to avoid thermal degradation of the PCL polymer, which typically begins above 220°C. Since PCL melts between 60 and 65°C, heating beyond 200°C is unnecessary for observing key transitions related to drug-polymer interactions, such as melting, crystallinity changes, and potential miscibility

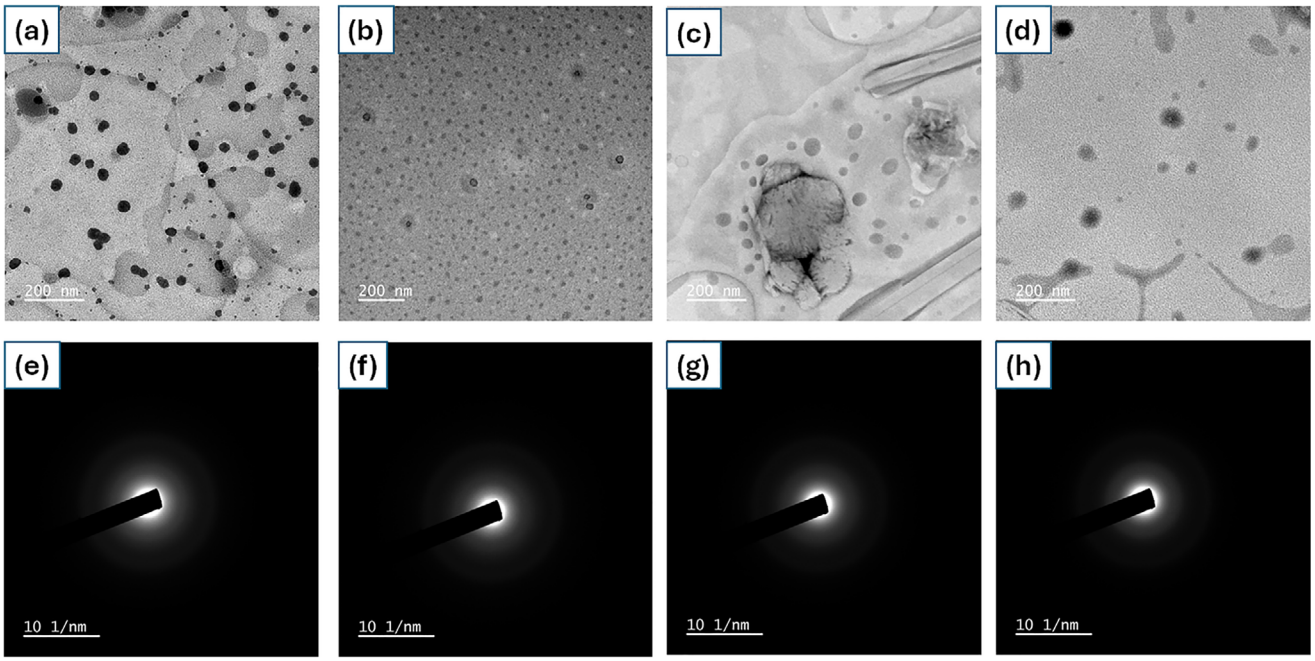

FIGURE 8 | TEM images of PCL NPs (a), PCL-BA NPs (b), PCL-TA NPs (c), and PCL-BA-TA NPs (d); SAED patterns of PCL NPs (e), PCL-BA NPs (f), PCL-TA NPs (g), and PCL-BA-TA NPs (h).

or amorphization of the encapsulated drug. Exceeding 200°C could cause polymer degradation, leading to thermal artifacts that might obscure or alter the interpretation of drug encapsulation behavior. Therefore, limiting the temperature range allows for accurate characterization of the nanocarriers while maintaining sample integrity.

Figure 9a shows a thermogram of BA, which displays three endothermic peaks at 70, 315, and 350°C. A small endothermic peak at 70°C is attributed to residual moisture or volatile impurities. A prominent peak at 315°C appears on the DSC curve of BA before decomposition begins, corresponding to its melting transition, which precedes degradation. After melting, BA undergoes thermal degradation at 350°C. The melting temperature indicated by the DSC curve aligns with the previously reported melting point of BA from thermo-optical analysis. Nicolov et al. [56] reported a strong endothermic peak at 313.63°C, attributed to the melting of BA, accompanied by its decomposition. These results further confirm that BA's melting point is high and that decomposition occurs. The DSC curve in Figure 9b shows that TA exhibits two endothermic peaks at 190 and 305°C. The first at 190°C is related to crystal and pre-melting, involving the rearrangement of the solid-state structure into a higher-entropy form in preparation for melting. The second peak at 305°C corresponds to the melting and decomposition of TA. Therefore, this major endothermic peak is attributed to melting with the simultaneous onset of decomposition.

This study describes a two-step heating process for PCL, PCL NPs, PCL-BA NPs, PCL-TA NPs, and PCL-BA-TA NPs. The initial heating of NPs was performed to remove residual excipients and assess the polymer's material properties. The thermal history was erased through cooling, followed by a second heating to determine the material's inherent characteristics. As shown in Figure 9c, the initial heating of PCL revealed a distinct endothermic peak at 65°C, indicating the melting or decomposition point, while PCL NPs, PCL-BA NPs, PCL-TA NPs, and PCL-BA-TA NPs displayed four broad, shorter endothermic peaks at 73.4, 73.9, 72.5, and 92.8°C. The shifts to higher temperatures compared to free PCL can be attributed to the nanoparticulate form of PCL, where polymer chains become more ordered and stabilized due to nanoscale confinement. Encapsulation promotes hydrophobic interactions between PCL and the triterpenoids (BA and TA), restricting chain mobility and increasing the melting point. Additionally, co-loading BA and TA appears to improve packing density within the PCL matrix. The combined triterpenoids foster stronger intermolecular interactions with PCL chains, forming more ordered, thermally stable microdomains, consistent with the significantly higher thermal transition temperature observed at 92.8°C. Cooling PCL, PCL NPs, PCL-BA NPs, PCL-TA NPs, and PCL-BA-TA NPs from 200 to −60°C results in an exothermic crystallization peak at 31.4°C for PCL, demonstrating its crystalline state, while the amorphous solidification of PCL NPs, PCL-BA NPs, PCL-TA NPs, and PCL-BA-TA NPs indicates their amorphous character, as shown in Figure 9d.

In the second heating cycle, the endotherms observed after the first heating for PCL NPs, PCL-BA NPs, PCL-TA NPs, and PCL-BA-TA NPs still show a single melting peak, as observed for neat PCL (Figure 9e). This behavior reflects the removal of the sample's thermal history by the first melt–cool cycle and subsequent recrystallization during cooling, which results in a more uniform PCL crystalline phase in the second heat. The appearance of a lower melting transition at 51.6°C during the second heating of drug-loaded formulations indicates that BA and TA are incorporated within the polymer matrix and influence polymer chain packing; drug molecules can act as plasticizers or disrupt crystal growth, leading to an increase in amorphous

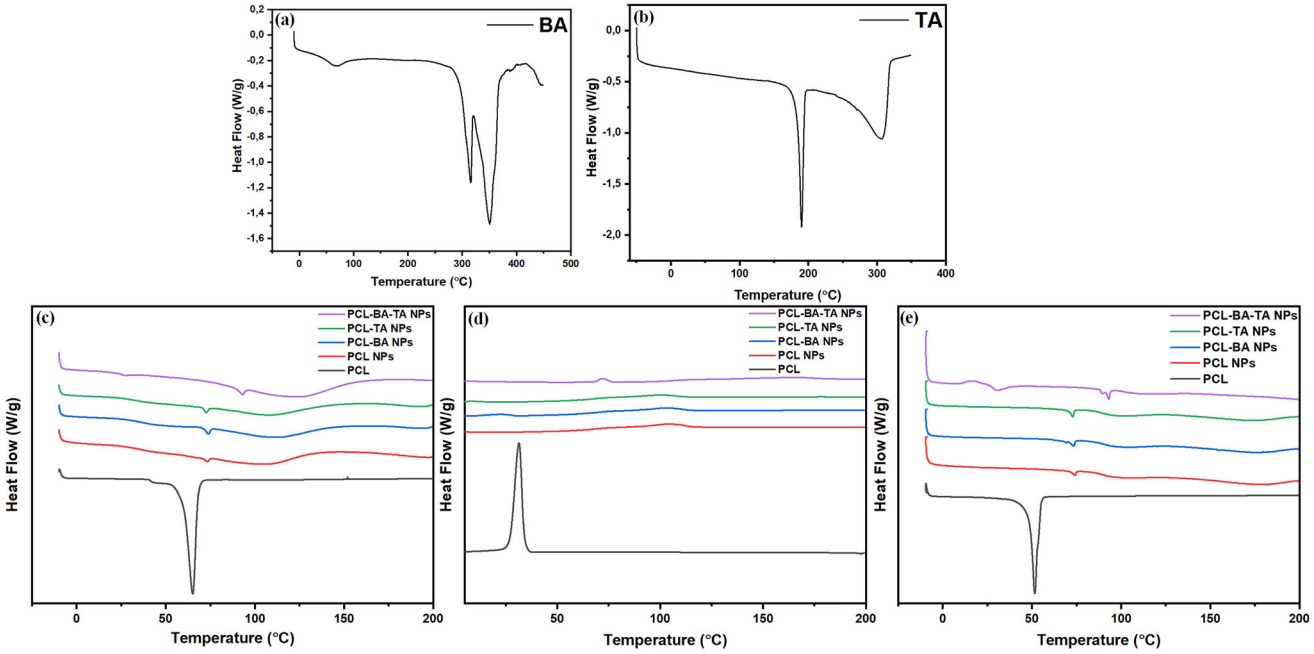

FIGURE 9 | DSC thermograms of (a) BA and (b) TA, (c) first heating of PCL, PCL NPs, PCL-BA NPs, PCL-TA NPs, and PCL-BA-TA NPs, (d) cooling of PCL, PCL NPs, PCL-BA NPs, PCL-TA NPs, and PCL-BA-TA NPs to −60 C after the first heating, and (e) second heating of PCL, PCL NPs, PCL-BA NPs, PCL-TA NPs, and PCL-BA-TA NPs.

content or defects in the PCL crystals and thus depress the observed melting temperature. Significantly, the presence of the drug in the matrix shifting from a crystalline to an amorphous form increases the dissolution rate and bioavailability because amorphous solids are thermodynamically more energetic and generally dissolve faster than their crystalline counterparts.

3.3 | In Vitro Release Profiles of BA and TA From PCL NPs

The controlled release behavior of phytochemical-loaded polymeric NPs is vital for optimizing therapeutic effectiveness. In this study, we examined the in vitro release profiles of PCL-encapsulated BA and TA in phosphate-buffered saline (PBS, pH 7.4) (Figure 10). The release profiles displayed a biphasic pattern typical of polymeric delivery systems [57]. An initial burst release occurred within the first 12 h, followed by a sustained release phase. Over 60% of BA and TA were released within the first 12 h, likely due to surface-associated drug, followed by a gradual, continuous release reaching 70–85% at 72 h. Burst release offers rapid therapeutic action by delivering a high initial drug concentration, which is beneficial for immediate pharmacological effects [58]. In contrast, sustained-release formulations maintain consistent drug levels over time, improving efficacy, reducing dosing frequency, and minimizing side effects [59]. Together, these profiles enable optimized drug delivery through controlled-release kinetics tailored to therapeutic needs. Notably, BA-loaded NPs showed a slightly faster release rate compared to TA-loaded NPs, possibly due to differences in hydrophobicity and molecular interaction with the PCL matrix. These findings demonstrate the potential of PCL NPs as effective carriers for the controlled delivery of hydrophobic triterpenoids such as BA and TA, providing sustained release suitable for therapeutic applications.

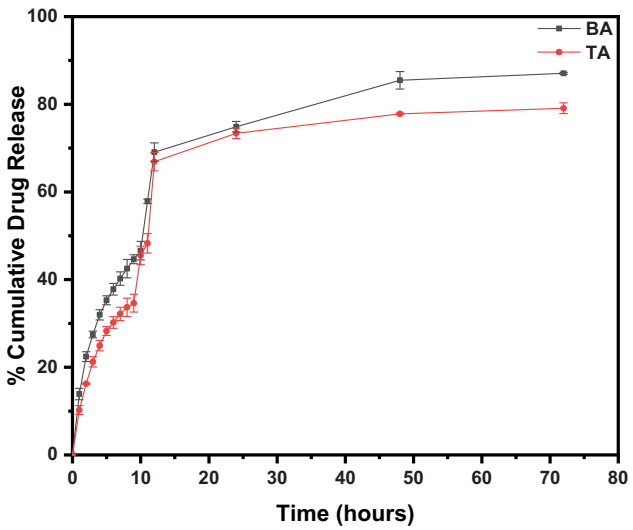

FIGURE 10 | In vitro release profiles of BA and TA drugs loaded PCL NPs in phosphate-buffered saline (pH 7.4) at 37°C.

3.4 | Antioxidant Activity

As shown in Figure 11, the antioxidant activities of BA, TA, their PCL-based nanoparticle formulations, and ascorbic acid were evaluated using the DPPH radical scavenging assay. Among the samples tested, PCL-BA-TA NPs exhibited the highest radical scavenging activity, which is due to hydroxyl and carboxylic

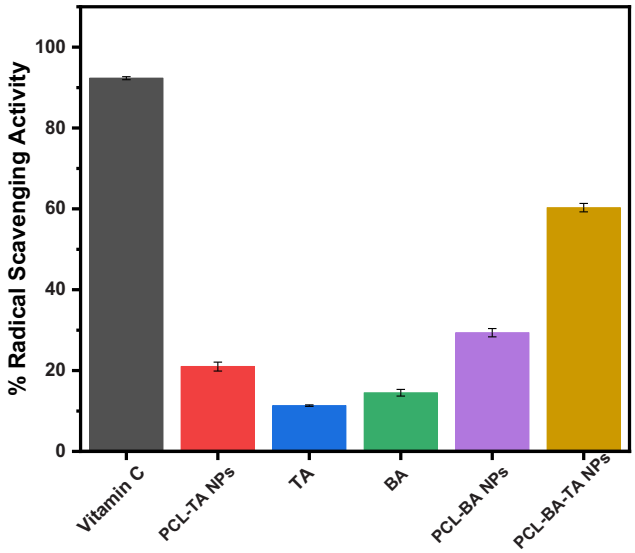

FIGURE 11 | Percentage of radical scavenging activity at 1 mg/mL of BA, TA, PCL-BA NPs, PCL-TA NPs, and PCL-BA-TA NPs compared to Ascorbic acid (vitamin C) positive control.

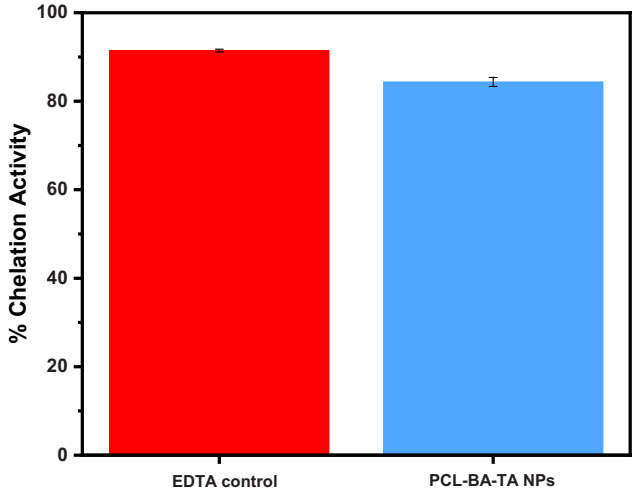

FIGURE 12 | Metal chelating activity of PCL-BA-TA NPs compared to the EDTA positive control at 1 mg/mL.

functional groups capable of donating hydrogen atoms and transferring electrons to neutralize free radicals. In contrast, the free compounds showed lower antioxidant activity, consistent with their hydrophobic nature and limited polar functionalities. Similar improvements in DPPH scavenging have been reported for PCL-based NPs. For example, Oliveira et al. [60] loaded a *Hypericum perforatum* fraction into PCL NPs and observed enhanced antioxidant activity compared to the free extract. This work encapsulated a plant extract containing quercetin/biapigenin into PCL NPs and demonstrated improved antioxidant and release properties compared with the free extract. Notably, in our current study, the co-loaded formulation showed a synergistic increase in free radical scavenging, likely due to increased solubility, better bioavailability, and controlled release of active molecules. The PCL-BA-TA NPs achieved approximately 60% DPPH scavenging activity, while the free compounds showed activities below 20%. Additionally, the scavenging efficiency of the co-loaded PCL NPs was comparable to that of ascorbic acid at higher concentrations. Ramzan et al. [61] demonstrated that PCL NPs co-loaded with quercetin and vitamin C achieved about 93% DPPH radical scavenging, significantly higher than many free analogues, supporting the idea of substantial enhancement through nanoparticulate PCL encapsulation. The notable antioxidant activity of the PCL-BA-TA NPs highlights the synergistic benefit of dual encapsulation within a biodegradable polymer carrier.

3.5 | Chelation Activity

Based on antioxidant evaluation, PCL-BA-TA NPs showed superior activity compared to individual loaded formulations and their free counterparts. This enhanced performance led to further investigation of their metal-chelation potential using Fe^{2+} chelation assays to better understand their antioxidant mechanisms. The co-loaded formulation demonstrated 80% chelating activity, comparable to the 90% chelation shown by the EDTA positive control, as depicted in Figure 12. The improved chelation may be due to the synergistic effects of BA and TA when encapsulated within the PCL matrix, potentially increasing solubility, stability, and bioavailability. Similar studies have indicated that BA and TA exhibit notable antioxidant and metal-chelating properties, helping to reduce oxidative stress and protect against free radical-induced cellular damage [62, 63]. These findings highlight the potential of PCL-BA-TA NPs as effective metal chelators and suggest their potential application in mitigating conditions associated with oxidative stress.

3.6 | Cytotoxic Evaluation of PCL Nanoparticles Loaded With Betulinic Acid and Taraxerol on HeLa and HepG2 Cancer Cells

The cytotoxic effects of BA, TA, PCL NPs, PCL-BA NPs, PCL-TA NPs, and PCL-BA-TA NPs on HeLa and HepG2 cancer cell lines, as shown in Figures 13 and 14, respectively, were evaluated. The free natural compounds showed limited anticancer activity in both cell types, mainly due to poor water solubility and limited bioavailability. Among them, BA exhibits slightly higher cytotoxicity than TA, likely due to structural differences that increase its lipophilicity and mitochondrial membrane affinity, thereby enhancing apoptosis induction. BA shows strong cytotoxicity across various cancer cell lines, primarily through the intrinsic (mitochondria-mediated) apoptotic pathway. In HeLa cells, BA induces excessive intracellular ROS, leading to mitochondrial membrane depolarization, the release of pro-apoptotic factors, such as cytochrome c, and the subsequent activation of initiator caspase-9 and executioner caspase-3, ultimately resulting in apoptosis.

In HepG2 cells, BA additionally triggers G2/M-phase cell-cycle arrest by disrupting cyclin-dependent kinase regulation, along with increased ROS production and mitochondrial dysfunction. However, the response is less potent than in HeLa cells, possibly due to enhanced metabolic detoxification and drug efflux activities characteristic of hepatic cancer cells. TA, although less potent than BA, induces cancer cell death through a

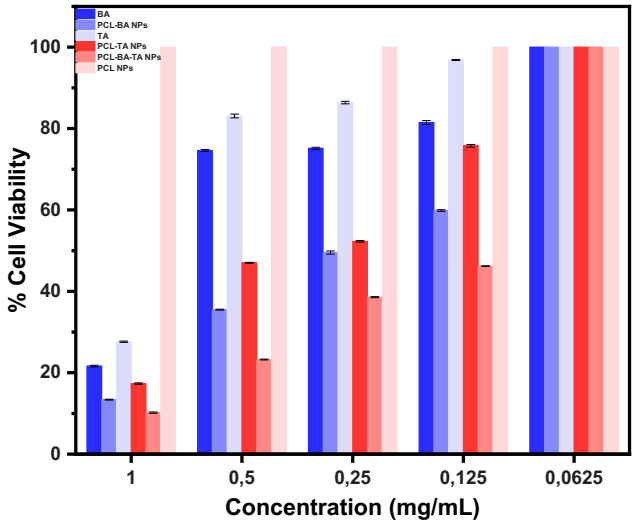

FIGURE 13 | The cytotoxic effects on HeLa cancer cell lines were evaluated by treating cells with BA. TA, PCL NPs, PCL-BA NPs, PCL-TA NPs, and PCL-BA-TA NPs at decreasing concentrations of 1, 0.5, 0.25, 0.125, and 0.0625 mg/mL for 48 h.

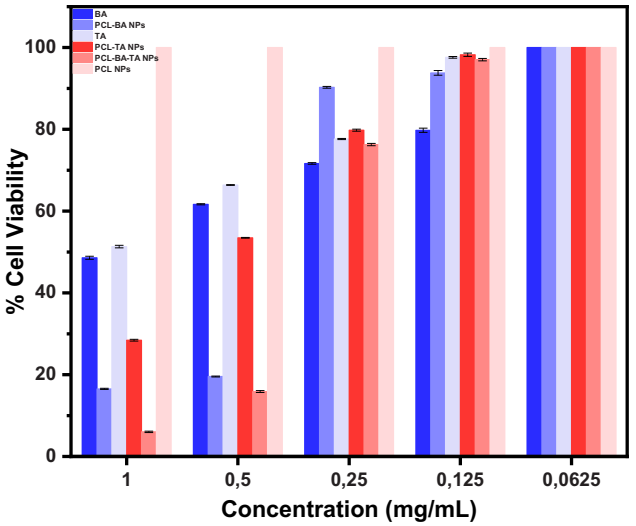

FIGURE 14 | The cytotoxic effects on HepG2 cancer cell lines were evaluated by treating cells with BA, TA, PCL NPs, PCL-BA NPs, PCL-TA NPs, and PCL-BA-TA NPs at decreasing concentrations of 1, 0.5, 0.25, 0.125, and 0.0625 mg/mL for 48 h.

combination of apoptosis modulation and anti-inflammatory signaling interference rather than serious direct mitochondrial damage. TA exerts anticancer effects by suppressing NF-κB signaling, reducing transcription of survival and anti-apoptotic genes, down-regulating anti-apoptotic Bcl-2, and up-regulating pro-apoptotic proteins such as Bax, thereby shifting the mitochondrial balance toward apoptosis. In HeLa cells, TA facilitates mitochondrial outer membrane permeabilization, promotes cytochrome c release, and activates downstream caspases, leading to apoptotic cell death. Additionally, TA-induced oxidative stress contributes to apoptosis, although to a lesser extent than BA. Nonetheless, the poor water solubility and bioavailability of both triterpenoids limit their intracellular accumulation, resulting in only moderate anticancer activity when administered in free form.

To address the solubility and bioavailability issues of these triterpenoids, they were encapsulated in PCL NPs, a biocompatible and biodegradable polymer recognized for controlled drug release [64]. The encapsulation of BA and TA within PCL NPs significantly enhanced their cytotoxic potential compared to the free compounds. This improvement is due to enhanced aqueous dispersibility, protection from premature degradation, prolonged intracellular retention, and enhanced endocytic uptake, all facilitated by the polymeric nanocarrier system. Notably, the PCL-BA-TA NPs exhibited the most pronounced cytotoxicity in both cell lines, suggesting a synergistic interaction between the two triterpenoids. This synergy likely arises from their complementary mechanisms for inducing apoptosis: BA induces robust mitochondrial dysfunction and caspase-dependent apoptosis, while TA amplifies apoptotic signaling by suppressing survival pathways and sensitizing cells to oxidative and mitochondrial stress. The study by Kumar et al. [65] provided compelling evidence that encapsulation in PLGA NPs can improve solubility, enable sustained release, and enhance the anticancer efficacy of hydrophobic triterpenoids such as BA against hepatic cancer, directly supporting the finding that polymeric nanoencapsulation boosts the activity of hydrophobic triterpenoids.

Despite using a different natural compound (naringenin), a significant study showed that PCL NPs can considerably increase cytotoxicity against HepG2 cells compared to the free compound, demonstrating that PCL is an effective carrier for enhancing hydrophobic phytochemical delivery and supporting the PCL findings [66]. Additionally, several studies indicate that co-loading a conventional chemotherapeutic with natural compounds into polymeric NPs can produce additive or synergistic anticancer effects, thereby improving cell killing compared to single-agent NPs. This confirms that PCL-BA-TA NPs exhibited increased cytotoxicity [67].

Notably, while all loaded formulations exhibited significant cytotoxicity in HeLa cells, their effectiveness was comparatively lower in HepG2 cells. The decreased sensitivity of HepG2 cells may be due to their inherent metabolic and defense mechanisms. Liver cells possess robust detoxification systems, including cytochrome P450 enzymes and efflux transporters such as P-gp, which can metabolize or export foreign compounds, thus limiting intracellular drug accumulation. Additionally, strong antioxidant systems in HepG2 cells (e.g., glutathione and catalase activity) can mitigate triterpenoid-induced oxidative stress, resulting in lower cytotoxicity compared to HeLa cells [68].

Importantly, PCL NPs showed minimal cytotoxicity in both cell lines, maintaining high cell viability. This confirms the biocompatibility and non-toxicity of PCL, an FDA-approved biodegradable polymer widely recognized for its safety in drug-delivery applications [69]. These findings demonstrate that PCL-based nanoformulations significantly boost the therapeutic potential of poorly soluble natural compounds. At the same time, the co-delivery of BA and TA provides mechanistically complementary and synergistic anticancer effects, suggesting a promising strategy for combination cancer therapy.

4 | Conclusions

The investigation into the therapeutic potential of BA and TA encapsulated within PCL nanocarriers has revealed promising multifunctional bioactivities, including antioxidant and antitumor effects. Both BA and TA, naturally derived pentacyclic triterpenoids, have long demonstrated notable pharmacological properties; however, their clinical application has been limited by poor aqueous solubility and bioavailability. PCL-based nanocarriers were used to address these limitations, thereby improving solubility, bioavailability, and sustained release profiles. In antioxidant tests, the PCL-encapsulated formulations showed superior radical-scavenging activity compared to their free forms, attributed to improved dispersion and sustained release of the active compounds. Most notably, the PCL-loaded BA, TA, and their combined formulation displayed strong antitumor effects against HeLa and HepG2 cell lines. The co-loaded nanocarriers performed better than individual formulations, indicating a synergistic interaction that effectively targeted multiple cancer cell pathways. Additionally, the PCL nanocarrier system not only improved the physicochemical properties of BA and TA but also significantly increased their biological activity in antioxidant and anticancer tests. These results highlight the potential of PCL-based co-delivery systems for developing multifunctional nanomedicines for integrated therapeutic use. Further in vivo studies and mechanistic research are needed to fully translate these promising in vitro results into clinical applications.

Author Contributions

Cyril Tlou Selepe: conceptualization, investigation, methodology, data curation, writing – original draft preparation, writing – review and editing, visualization. **Khanyisile Sheer Dhlamini**: validation, writing, review, and editing. **Lesego Tshweu**: validation, writing, review, and editing. **Zandile Nxumalo**: resources, validation, writing, review, and editing. **Nkoana Ishmael Mongalo**: resources, validation, writing, review, and editing. **Maropeng Vellry Raletsena**: validation, writing, review, and editing. **Lusisizwe Kwezi**: conceptualization, writing, review and editing, supervision. **Bathabile Ramalapa**: conceptualization, methodology, formal analysis, resources, writing – original draft preparation, writing – review and editing, supervision, project administration. **Suprakas Sinha Ray**: conceptualization, resources, writing – review and editing, supervision, project administration, funding acquisition.

Acknowledgements

The authors acknowledge financial support from the Department of Science and Innovation (grant number C6A0056).

Conflicts of Interest

The authors declare no conflict of interest.

Data Availability Statement

The data that support the findings of this study are available from the corresponding author upon reasonable request.

References

1. J. P. Silva and O. P. Coutinho, "Free Radicals in the Regulation of Damage and Cell Death-Basic Mechanisms and Prevention," *Drug Discoveries & Therapeutics* 4, no. 3 (2010): 144.

2. J. Lugrin, N. Rosenblatt-Velin, R. Parapanov, and L. Liaudet, "The Role of Oxidative Stress during Inflammatory Processes," *Biological Chemistry* 395, no. 2 (2014): 203–230, https://doi.org/10.1515/hsz-2013-0241.

3. F. B. Mullauer, J. H. Kessler, and J. P. Medema, "Betulinic Acid, a Natural Compound With Potent Anticancer Effects," *Anti-cancer drugs* 21, no. 3 (2010): 215–227, https://doi.org/10.1097/CAD.0b013e3283357c62.

4. R. Watkins, L. Wu, C. Zhang, R. M. Davis, and B. Xu, "Natural Product-Based Nanomedicine: Recent Advances and Issues," *International Journal of Nanomedicine* 10 (2015): 6055–6074.

5. H. Lou, H. Li, S. Zhang, H. Lu, and Q. Chen, "A Review on Preparation of Betulinic Acid and Its Biological Activities," *Molecules* 26, no. 18 (2021): 5583, https://doi.org/10.3390/molecules26185583.

6. K.-D. Kim, H.-Y. Jung, H. Ryu, et al., "Betulinic Acid Inhibits High-Fat Diet-Induced Obesity and Improves Energy Balance by Activating AMPK," *Nutrition, Metabolism and Cardiovascular Diseases* 29, no. 4 (2019): 409–420, https://doi.org/10.1016/j.numecd.2018.12.001.

7. A. Hordyjewska, A. Ostapiuk, A. Horecka, and J. Kurzepa, "Betulin and Betulinic Acid: Triterpenoids Derivatives With a Powerful Biological Potential," *Phytochemistry Reviews* 18 (2019): 929–951, https://doi.org/10.1007/s11101-019-09623-1.

8. R. Mukherjee, V. Kumar, S. K. Srivastava, S. K. Agarwal, and A. C. Burman, "Betulinic Acid Derivatives as Anticancer Agents: Structure Activity Relationship," *Anti-Cancer Agents in Medicinal Chemistry* 6, no. 3 (2006): 271–279, https://doi.org/10.2174/187152006776930846.

9. J. Y. Kim, H.-M. Koo, and D. S. Kim, "Development of C-20 Modified Betulinic Acid Derivatives as Antitumor Agents," *Bioorganic & Medicinal Chemistry Letters* 11, no. 17 (2001): 2405–2408.

10. A. Saneja, L. Sharma, R. D. Dubey, et al., "Synthesis, Characterization and Augmented Anticancer Potential of PEG-Betulinic Acid Conjugate," *Materials Science and Engineering: C* 73 (2017): 616–626, https://doi.org/10.1016/j.msec.2016.12.109.

11. L. Dai, D. Li, J. Cheng, et al., "Water soluble multiarm-polyethylene glycol–betulinic acid prodrugs: Design, synthesis, and in vivo effectiveness," *Polymer Chemistry* 5, no. 19 (2014): 5775–5783, https://doi.org/10.1039/C4PY00648H.

12. X. Yao, G. Li, Q. Bai, H. Xu, and C. Lü, "Taraxerol Inhibits LPS-Induced Inflammatory Responses through Suppression of TAK1 and Akt Activation," *International Immunopharmacology* 15, no. 2 (2013): 316–324, https://doi.org/10.1016/j.intimp.2012.12.032.

13. K. Sharma and R. Zafar, "Simultaneous Estimation of Taraxerol and Taraxasterol in Root Callus Cultures of Taraxacum Officinale Weber," *International Journal of Pharmacognosy and Phytochemical Research* 6, no. 3 (2014): 540–546.

14. A. A. Mus, L. P. W. Goh, H. Marbawi, and J. A. Gansau, "The Biosynthesis and Medicinal Properties of Taraxerol," *Biomedicines* 10, no. 4 (2022): 807, https://doi.org/10.3390/biomedicines10040807.

15. U.-K. Choi, O.-H. Lee, J. H. Yim, et al., "Hypolipidemic and Antioxidant Effects of Dandelion (Taraxacum officinale) Root and Leaf on Cholesterol-Fed Rabbits," *International Journal of Molecular Sciences* 11, no. 1 (2010): 67–78, https://doi.org/10.3390/ijms11010067.

16. B. Tan, H. Shi, G. Ji, and J. Xie, "Effects of taraxerol and taraxeryl acetate on cell cycle and apoptosis of human gastric epithelial cell line AGS," *Journal of Chinese Integrative Medicine* 9, no. 6 (2011): 638–642, https://doi.org/10.3736/jcim20110610.

17. D. Naik, A. Mujumdar, R. Waghole, et al., "Taraxer-14-en-3β-ol, an Anti-inflammatory Compound From Sterculia Foetida L," *Planta Medica* 70, no. 01 (2004): 68–69.

18. B. Singh, P. Sahu, and M. Sharma, "Anti-inflammatory and Antimicrobial Activities of Triterpenoids From Strobilanthes Callosus Nees," *Phytomedicine* 9, no. 4 (2002): 355–359, https://doi.org/10.1078/0944-7113-00143.

19. R. Csuk, "Betulinic Acid and Its Derivatives: A Patent Review," *Expert Opinion on Therapeutic Patents* 24, no. 8 (2014): 913–923.

20. T. E. Berté, A. P. Dalmagro, P. L. Zimath, et al., "Taraxerol as a Possible Therapeutic Agent on Memory Impairments and Alzheimer's Disease: Effects against Scopolamine and Streptozotocin-Induced Cognitive Dysfunctions," *Steroids* 132 (2018): 5–11.

21. A. Kaps, P. Gwiazdoń, and E. Chodurek, "Nanoformulations for Delivery of Pentacyclic Triterpenoids in Anticancer Therapies," *Molecules (Basel, Switzerland)* 26, no. 6 (2021): 1764, https://doi.org/10.3390/molecules26061764.

22. I. Mierina, R. Vilskersts, and M. Turks, "Delivery Systems for Birch-Bark Triterpenoids and Their Derivatives in Anticancer Research," *Current Medicinal Chemistry* 27, no. 8 (2020): 1308–1336, https://doi.org/10.2174/0929867325666180530095657.

23. T. K. Dash and V. B. Konkimalla, "Polymeric Modification and its Implication in Drug Delivery: Polycaprolactone (pcl) as a Model Polymer," *Molecular Pharmaceutics* 9, no. 9 (2012): 2365–2379.

24. O. Mitxelena-Iribarren, M. Riera-Pons, S. Pereira, et al., "Drug-loaded PCL Electrospun Nanofibers as Anti-Pancreatic Cancer Drug Delivery Systems," *Polymer Bulletin* 80, no. 7 (2023): 7763–7778, https://doi.org/10.1007/s00289-022-04425-6.

25. P. Grossen, D. Witzigmann, S. Sieber, and J. Huwyler, "PEG-PCL-Based Nanomedicines: A Biodegradable Drug Delivery System and Its Application," *Journal of Controlled Release* 260 (2017): 46–60, https://doi.org/10.1016/j.jconrel.2017.05.028.

26. Y. Ma, Y. Zheng, X. Zeng, et al., "Novel Docetaxel-Loaded Nanoparticles Based on PCL-Tween 80 Copolymer for Cancer Treatment," *International Journal of Nanomedicine* 6 (2011): 2679–2688.

27. A. T. Alex, A. Joseph, G. Shavi, J. V. Rao, and N. Udupa, "Development and Evaluation of Carboplatin-Loaded PCL Nanoparticles for Intranasal Delivery," *Drug Delivery* 23, no. 7 (2016): 2144–2153, https://doi.org/10.3109/10717544.2014.948643.

28. H. Ahmadi and V. Haddadi-Asl, "Curcumin-loaded Polycaprolactone Nanoparticles Prepared by Emulsion Evaporation Stabilized with a pH - responsive Emulsifier," *Polymer Engineering & Science* 65, no. 6 (2025): 3147–3162, https://doi.org/10.1002/pen.27205.

29. D. P.-A. M. Luisa, R.-M. Griselda, M.-L. Valentín, et al., "Curcumin-Loaded Poly-ε-Caprolactone Nanoparticles Show Antioxidant and Cytoprotective Effects in the Presence of Reactive Oxygen Species," *Journal of Bioactive and Compatible Polymers* 35, no. 3 (2020): 270–285, https://doi.org/10.1177/0883911520921499.

30. L. Cabeza, R. Ortiz, J. Prados, et al., "Improved Antitumor Activity and Reduced Toxicity of Doxorubicin Encapsulated in Poly(ε-caprolactone) Nanoparticles in Lung and Breast Cancer Treatment: An in Vitro and in Vivo Study," *European Journal of Pharmaceutical Sciences* 102 (2017): 24–34, https://doi.org/10.1016/j.ejps.2017.02.026.

31. N. Mongalo, L. McGaw, J. Finnie, and J. Van Staden, "Isolation and characterization of antimicrobial and anti-inflammatory triterpenoids From the acetone extract of Grewia flava DC. (Malvaceae) roots," *South African Journal of Botany* 149 (2022): 87–95, https://doi.org/10.1016/j.sajb.2022.05.048.

32. J. Douros and M. Suffness, "The National Cancer Institute's Natural Products Antineoplastic Development Program," *Cancer Research* 70 (1980): 21–44.

33. C. T. Selepe, K. S. Dhlamini, L. Tshweu, L. Kwezi, B. Ramalapa, and S. S. Ray, "Development and Evaluation of Poly(Lactic-Co-Glycolic Acid) Encapsulated Betulinic Acid Nanocarrier for Improved Anti-Tumor Efficacy," *Macromolecular Materials and Engineering* 310, no. 2 (2025): 2400283, https://doi.org/10.1002/mame.202400283.

34. M. Lebeloane, I. Famuyide, K. Kgosana, et al., "Anti-Inflammatory Activity of Seven Plant Species With Potential Use as Livestock Feed Additives," *South African Journal of Botany* 167 (2024): 322–332, https://doi.org/10.1016/j.sajb.2024.02.017.

35. S. Baliyan, R. Mukherjee, A. Priyadarshini, et al., "Determination of Antioxidants by DPPH Radical Scavenging Activity and Quantitative Phytochemical Analysis of Ficus Religiosa," *Molecules (Basel, Switzerland)* 27, no. 4 (2022): 1326, https://doi.org/10.3390/molecules27041326.

36. G. Alagumanivasagam, R. Pasupathy, A. Kottaimuthu, and R. Manavalan, "A Review on in-vitro Antioxidant Methods," *International Journal of Pharmacy and Pharmaceutical Sciences* 1, no. 2 (2012): 662–674.

37. V. Nithyamol Kalappurakkal, D. Bhattacharya, S. Chakravarty, and M. Venkata Uppuluri, "Isolation, Synthesis and AC hE Inhibitory Potential of some Novel Cinnamyl Esters of Taraxerol, the Major Metabolite of the Mangrove Bruguiera Cylindrica," *Chemistry & Biodiversity* 15, no. 4 (2018): 1800008, https://doi.org/10.1002/cbdv.201800008.

38. K. Sharma and R. Zafar, "Occurrence of Taraxerol and Taraxasterol in Medicinal Plants," *Pharmacognosy Reviews* 9, no. 17 (2015): 19.

39. Y. Guo, Z. Han, J. Zhang, Y. Lu, C. Li, and G. Liu, "Development of a High-Speed and Ultrasensitive UV/Vis-CM for Detecting Total Triterpenes in Traditional Chinese Medicine and Its Application," *Heliyon* 10, no. 11 (2024): e32239, https://doi.org/10.1016/j.heliyon.2024.e32239.

40. G. Zhao, W. Yan, and D. Cao, "Simultaneous Determination of Betulin and Betulinic Acid in White Birch Bark Using RP-HPLC," *Journal of Pharmaceutical and Biomedical Analysis* 43, no. 3 (2007): 959–962, https://doi.org/10.1016/j.jpba.2006.09.026.

41. S. Kaennakam, J. Sichaem, S. Khumkratok, P. Siripong, and S. Tippyang, "A New Taraxerol Derivative from the Roots of Microcos Tomentosa," *Natural Product Communications* 8, no. 10 (2013): 1300801007, https://doi.org/10.1177/1934578X1300801007.

42. N. Sakurai, Y. Yaguchi, and T. Inoue, "Triterpenoids From Myrica Rubra," *Phytochemistry* 26, no. 1 (1986): 217–219, https://doi.org/10.1016/S0031-9422(00)81515-0.

43. C. Valente, M. Pedro, A. Duarte, M. S. Nascimento, P. M. Abreu, and M. J. Ferreira, "Bioactive Diterpenoids, a New Jatrophane and Two Ent-abietanes, and Other Constituents From Euphorbia Pubescens," *Journal of Natural Products* 67, no. 5 (2004): 902–904, https://doi.org/10.1021/np0400048.

44. S. S. Kumar, "Formulation and Characterization of Noscapine-Loaded Polycaprolactone Nanoparticles," *Asian Journal of Pharmaceutics* 13, no. 01 (2019): 10–18.

45. D. J. Pochapski, C. Carvalho dos Santos, G. W. Leite, S. H. Pulcinelli, and C. V. Santilli, "Zeta Potential and Colloidal Stability Predictions for Inorganic Nanoparticle Dispersions: Effects of Experimental Conditions and Electrokinetic Models on the Interpretation of Results," *Langmuir* 37, no. 45 (2021): 13379–13389, https://doi.org/10.1021/acs.langmuir.1c02056.

46. M. Alkholief, M. A. Kalam, M. K. Anwer, and A. Alshamsan, "Effect of Solvents, Stabilizers and the Concentration of Stabilizers on the Physical Properties of Poly(d,l-lactide-co-glycolide) Nanoparticles: Encapsulation, In Vitro Release of Indomethacin and Cytotoxicity Against HepG2-Cell," *Pharmaceutics* 14, no. 4 (2022): 870, https://doi.org/10.3390/pharmaceutics14040870.

47. K. Phillipson, J. N. Hay, and M. J. Jenkins, "Thermal Analysis FTIR Spectroscopy of Poly(ε-caprolactone)," *Thermochimica Acta* 595 (2014): 74–82, https://doi.org/10.1016/j.tca.2014.08.027.

48. S. Cîntă-Pînzaru, C. A. Dehelean, C. Soica, M. Culea, and F. Borcan, "Evaluation and Differentiation of the Betulaceae Birch Bark Species and Their Bioactive Triterpene Content Using Analytical FT-Vibrational Spectroscopy and GC-MS," *Chemistry Central Journal* 6 (2012): 1–12.

49. K. Somarathinam, S. Gunalan, A. Sailapathi, et al., "Antihypertensive Effects of Pentacyclic Triterpenoid From Convolvulus Pluricaulis and Its Plausible Mechanism of Action Hypothesizing Its Selectivity Targeting Mineralocorticoid Receptor of RAAS," *Phytomedicine Plus* 3, no. 1 (2023): 100408, https://doi.org/10.1016/j.phyplu.2023.100408.

50. M. M. Badran, A. H. Alomrani, G. I. Harisa, A. E. Ashour, A. Kumar, and A. E. Yassin, "Novel Docetaxel Chitosan-Coated PLGA/PCL Nanoparticles With Magnified Cytotoxicity and Bioavailability," 106 (2018): 1461–1468.

51. X. Wang, H. Zhao, L.-S. Turng, and Q. Li, "Crystalline Morphology of Electrospun Poly (ε-caprolactone)(PCL) Nanofibers," *Industrial & Engineering Chemistry Research* 52, no. 13 (2013): 4939–4949, https://doi.org/10.1021/ie302185e.

52. J. M. Tan, G. Karthivashan, P. Arulselvan, S. Fakurazi, and M. Z. Hussein, "Characterization and in Vitro Studies of the Anticancer Effect of Oxidized Carbon Nanotubes Functionalized With Betulinic Acid," *Drug Design, Development and Therapy* 8 (2014): 2333–2343, https://doi.org/10.2147/DDDT.S70650.

53. K. Somarathinam, S. Gunalan, A. Sailapathi, et al., "Antihypertensive Effects of Pentacyclic Triterpenoid From Convolvulus Pluricaulis and Its Plausible Mechanism of Action Hypothesizing Its Selectivity Targeting Mineralocorticoid Receptor of RAAS," *Phytomedicine Plus* 3, no. 1 (2023): 100408, https://doi.org/10.1016/j.phyplu.2023.100408.

54. J. H. Park, D. I. Kim, S. G. Hong, H. Seo, J. Kim, G. D. Moon, and D. C. Hyun, "Poly(ε-caprolactone) (PCL) Hollow Nanoparticles With Surface Sealability and on-Demand Pore Generability for Easy Loading and NIR Light-Triggered Release of Drug," *Pharmaceutics* 11, no. 10 (2019): 528, https://doi.org/10.3390/pharmaceutics11100528.

55. A. Venkateshaiah, V. V. T. Padil, M. Nagalakshmaiah, S. Waclawek, M. Černík, and R. S. Varma, "Microscopic Techniques for the Analysis of Micro and Nanostructures of Biopolymers and Their Derivatives," *Polymers* 12, no. 3 (2020): 512, https://doi.org/10.3390/polym12030512.

56. M. Nicolov, R. M. Ghiulai, M. Voicu, et al., "Cocrystal Formation of Betulinic Acid and Ascorbic Acid: Synthesis, Physico-Chemical Assessment, Antioxidant, and Antiproliferative Activity," 7 (2019): 92.

57. M. M. Fard and A. M. Fard, "Investigation of Drug Release from a Biodegradable Biphasic Polymer System," *Eurasian Journal of Science and Technology* 2, no. 1 (2022): 1–13.

58. F. Danhier, E. Ansorena, J. M. Silva, R. Coco, A. L. Breton, and V. Préat, "PLGA-Based Nanoparticles: An Overview of Biomedical Applications," *Journal of Controlled Release* 161, no. 2 (2012): 505–522, https://doi.org/10.1016/j.jconrel.2012.01.043.

59. H. K. Makadia and S. J. Siegel, "Poly Lactic-co-Glycolic Acid (PLGA) as Biodegradable Controlled Drug Delivery Carrier," *Polymers* 3, no. 3 (2011): 1377–1397, https://doi.org/10.3390/polym3031377.

60. A. I. Oliveira, C. Pinho, P. Fonte, B. Sarmento, and A. C. P. Dias, "Development, Characterization, Antioxidant and Hepatoprotective Properties of Poly(Ɛ-caprolactone) Nanoparticles Loaded With a Neuroprotective Fraction of Hypericum Perforatum," *International Journal of Biological Macromolecules* 110 (2018): 185–196, https://doi.org/10.1016/j.ijbiomac.2017.10.103.

61. N. Ramzan, M. Azeem, K. Mahmood, et al., "Cellular and Non-cellular Antioxidant Properties of Vitamin E–Loaded Metallic-Quercetin/Polycaprolactone Nanoparticles for the Treatment of Melanogenesis," *Aaps Pharmscitech [Electronic Resource]* 24, no. 6 (2023): 141, https://doi.org/10.1208/s12249-023-02588-7.

62. A. H. Aodah, S. Devi, F. K. Alkholifi, H. S. Yusufoglu, A. I. Foudah, and A. Alam, "Effects of Taraxerol on Oxidative and Inflammatory Mediators in Isoproterenol-Induced Cardiotoxicity in an Animal Model," *Molecules (Basel, Switzerland)* 28, no. 10 (2023): 4089, https://doi.org/10.3390/molecules28104089.

63. M. J. Kim, H.-G. Kang, S.-B. Jeon, et al., "The Antioxidant Betulinic Acid Enhances Porcine Oocyte Maturation through Nrf2/Keap1 Signaling Pathway Modulation," *PLoS ONE* 19, no. 10 (2024): 0311819, https://doi.org/10.1371/journal.pone.0311819.

64. R. El Yousfi, M. Brahmi, M. Dalli, et al., "Recent Advances in Nanoparticle Development for Drug Delivery: A Comprehensive Review of Polycaprolactone-Based Multi-Arm Architectures," *Polymers* 15, no. 8 (2023): 1835, https://doi.org/10.3390/polym15081835.

65. P. Kumar, A. K. Singh, V. Raj, et al., "Poly(lactic-co-glycolic acid)-loaded Nanoparticles of Betulinic Acid for Improved Treatment of Hepatic Cancer: Characterization, in vitro and in vivo Evaluations," *International Journal of Nanomedicine* 13 (2018): 975–990, https://doi.org/10.2147/IJN.S157391.

66. B. Rabha, K. K. Bharadwaj, N. Boro, et al., "Cheilocostus Speciosus Extract-Assisted Naringenin-Encapsulated Poly-ε-caprolactone Nanoparticles: Evaluation of Anti-proliferative Activities," *Green Chemistry* 23, no. 19 (2021): 7701–7711, https://doi.org/10.1039/D1GC02260A.

67. T. Saikia, P. Rajak, B. P. Sahu, and L. Patowary, "Enhanced Lung Cancer Therapy via Co-Encapsulation of Docetaxel and Betulinic Acid," *Drugs and Drug Candidates* 3, no. 3 (2024): 566–597, https://doi.org/10.3390/ddc3030033.

68. A. C. Rodrigues, R. Curi, F. D. V. Genvigir, M. H. Hirata, and R. D. C. Hirata, "The Expression of Efflux and Uptake Transporters Are Regulated by Statins in Caco-2 and HepG2 Cells," *Acta Pharmacologica Sinica* 30, no. 7 (2009): 956–964, https://doi.org/10.1038/aps.2009.85.

69. A. Bhadran, T. Shah, G. K. Babanyinah, et al., "Recent Advances in Polycaprolactones for Anticancer Drug Delivery," *Pharmaceutics* 15, no. 7 (2023): 1977, https://doi.org/10.3390/pharmaceutics15071977.